3D Meshless Prostate Segmentation and Registration in Image Guided Radiotherapy

Ting Chen[1], Sung Kim[2], Jinghao Zhou[2], Dimitris Metaxas[3], Gunaretnam Rajagopal[1], and Ning Yue[2]

[1] Bioinformatics Core, Cancer Institute of New Jersey, University of Medicine and Dentistry of New Jersey, New Brunswick, NJ, USA
[2] Radiation Oncology Department, Cancer Institute of New Jersey, University of Medicine and Dentistry of New Jersey, New Brunswick, NJ, USA
[3] Computer Science Department, Rutgers University, Piscataway, NJ, USA

Abstract. Image Guided Radiation Therapy (IGRT) improves radiation therapy for prostate cancer by facilitating precise radiation dose coverage of the object of interest, and minimizing dose to adjacent normal organs. In an effort to optimize IGRT, we developed a fast segmentation-registration-segmentation framework to accurately and efficiently delineate the clinically critical objects in Cone Beam CT images obtained during radiation treatment. The proposed framework started with deformable models automatically segmenting the prostate, bladder, and rectum in planning CT images. All models were built around seed points and involved in the CT image under the influence of image features using the level set formulation. The deformable models were then converted into meshless point sets and underwent a 3D non rigid registration from the planning CT to the treatment CBCT. The motion of deformable models during the registration was constrained by the global shape prior on the target surface during the deformation. The meshless formulation provided a convenient interface between deformable models and the image feature based registration method. The final registered deformable models in the CBCT domain were further refined using the interaction between objects and other available image features. The segmentation results for 15 data sets has been included in the validation study, compared with manual segmentations by a radiation oncologist. The automatic segmentation results achieved a satisfactory convergence with manual segmentations and met the speed requirement for on line IGRT.

1 Introduction

One out of every four cancers diagnosed among American men is prostate cancer, and prostate cancer is estimated to cause the death of 28,660 males in North American in 2008 [1]. Radiation Therapy (RT) has been widely accepted as an effective treatment modality for prostate cancer. RT uses high energy photon beams to deposit high doses of radiation in the prostate to kill tumor cells. However, high dose radiation can also cause short and long term toxicity to adjacent normal organs, e.g., the rectum and bladder. Intensity Modulated Radiation

G.-Z. Yang et al. (Eds.): MICCAI 2009, Part I, LNCS 5761, pp. 43–50, 2009.

Therapy (IMRT) [2] is a relatively new modality that uses multiple beams and fluence modulations so that high dose is deposited to the prostate and relatively low dose to adjacent normal organs. The RT is based on the position of the prostate and surrounding organs at the time of CT simulation. Therefore, the accuracy of subsequent RT treatments is predicated on reproducing the prostate and surrounding organs' position in space at CT simulation during the daily RT treatment. The reproduction of the position is not trivial, as RT can last for eight weeks or more. Errors can be introduced due to changes in patient position, size of prostate, varying filling of the rectum or bladder. To guarantee that the prostate receives adequate dose, a margin is added to the target volume to form the Planned Target Volume (PTV), the volume to which high radiation dose is directed. Increasing the margin to the PTV, while increasing the odds of adequately treating the prostate, also adversely increases radiation dose to surrounding normal organs. Hence the need for IGRT (Image Guided Radiotherapy) [3] [4], which allows one to minimize the size of the PTV while still ensuring high dose to the prostate. One means of IGRT uses state of the art Cone Beam CT (CBCT) to acquire online treatment verification images. The main drawback of this method is that it currently requires manual segmentation and registration between the planning CT scan and the daily CBCT images, a cumbersome and time consuming task. Therefore, a fast, efficient segmentation and registration method would be extremely helpful clinically.

Many efforts have been made to develop algorithms for automatic CT and CBCT prostate segmentation [5] [6] [7]. However, interactive manual segmentations using tools with graphics user interface are still assumed to be the most reliable and time efficient means until now. Major difficulties that complicate the research in this direction include: 1) low saliency of boundary between the prostate and the adjacent organs; 2) gray scale inhomogeneity within the prostate; and 3) the visual artifacts generated by implanted seeds. A particular problem in segmenting CBCT images is that the noise-to-signal ratio is relatively high, and there is a strong demand from clinicians for high speed segmentation in order to adjust treatment plans in real time. Costa used [6] coupled deformable models to simultaneously segment the prostate and the bladder. However, the use of the Principal Component Analysis was rather empirical without a solid validation considering the relatively small testing group. Greene [8] developed a registration-segmentation framework for aligning between the planning CT and the treatment CBCT, but no explicit explanation was given regarding the segmentation method (especially for CBCT). This raises questions regarding the applicability of the method for real time IGRT data analysis. Another algorithm [9] used a Finite Element Method based framework to segment and validate prostate cancer data. The method was based on a mesh structure, which limited its flexibility when analyzing data with nonuniform deformations. We propose in this paper a segmentation-registration-segmentation framework to retrieve clinically critical objects in CT and CBCT data, in order to augment the potential of IGRT for prostate cancer. We will elaborate our methods in section 2 and present the experimental and validation results in section 3. We make our conclusions in section 4.

2 Method

In our framework, we focus on the segmentation of the prostate, bladder, and rectum. All images are pre-processed so that air regions in the rectum are masked with similar pixel values as the surrounding tissue during the registration. In CT images, models are initialized at seed points in the target organs.

2.1 Multi-object Level Set Models in CT

Three objects (prostate, bladder, and rectum) are modeled as level sets [10] using distance functions ϕ: which equals to 0 on the surface, greater than 0 inside and less than 0 outside. The intensity distribution for pixels inside each object are then calculated using nonparametric models in order to obtain the probabilistic density functions p_{ij} of arbitrary pixel j belonging to object i. We also compute the gradient map and the magnitude of gradient in the image domain. The segmentation process is of multiple steps. In each iteration, to determine the optimal classification, level set models representing different organs evolve and compete with each other for pixels. Each model evolves under the impact of three influences: 1) the inflation force based on the total gradient magnitude within the model volume; 2) the local image force at each pixel based on the probability function; and 3) the surface smoothness constraint based on the surface curvature $\nabla \cdot \frac{\nabla \phi}{\|\nabla \phi\|}$. To make the segmentation process more efficient, the model evolution and competition only take place in a narrow band around model surface, where $min(\phi_i) < \varepsilon$. We empirically choose $\varepsilon = 2$. For each pixel j in the narrow band, the value for $\phi(j)$ is recomputed using the following equation:

$$\frac{d\phi_i}{dt} = \left[\lambda_1 M_i + \nabla\lambda_2 P_i \cdot \left(\frac{\nabla\phi_i}{\|\nabla\phi_i\|}\right) - (\lambda_2 P_i + \lambda_3)\nabla \cdot \left(\frac{\nabla\phi_i}{\|\nabla\phi_i\|}\right)\right] \delta_\varepsilon(\phi_i) \qquad (1)$$

where $\delta_\varepsilon(\phi_i)$ is the regularized delta function, M_i is the inflation term derived from the gradient magnitude inside the object i, P_i is a function derived from the intensity probability competition as described in the following paragraph, and λ_3 is the weight for the smoothness on the object surface.

The competition of models are reflected by the second term on the right hand side of equation 1. The value of P is different from the probability of a pixel j belonging to object i (denoted by p_{ij}). First the value of P_{ij} is changed to $p_{ij} - \max p_{kj}$, where $k \in \{1, 2, 3\}$ and $k \neq i$. Second, at pixels with more than one $\phi_i > 0$, which equivalent to the overlapping between models, a new negative force source is introduced to locally decrease the value of both phi_i. The first modification sets the priority of models in the competition for pixels. The second modification enforces that there will be no overlapping in the segmentation result. Also for images with implanted seeds, which appear as bright spots in the image, we use local masks to block them so that $\lambda_2 = 0$ around the seeds. The segmentation results using the level set models can achieve a satisfactory accuracy. They serve as starting points for the registration process.

2.2 CT to CBCT Registration

Automating IGRT requires registration between CT and CBCT and also segmentation in each CBCT data set. In a previous research paper [8], segmentations of both the CT and the CBCT data were performed first, and then were used to guide the registration. However, we chose to analyze the data in the reverse order: registration first and the outcome is used to guide the CBCT segmentation. Major considerations behind our design are: 1) CBCT quality is typically inferior to that of CT and may deteriorate the outcome if the unreliable CBCT segmentation was used as input of registration. Therefore it is better to perform CT segmentation first, then register CT to CBCT, and finally improve the CBCT segmentation. Doing CT and CBCT segmentation and then registering would lead to error prone registration; and 2) registration provides an initialization close enough to the desired image feature, that it can speed up the CBCT segmentation process and therefore improves the overall efficiency of the IGRT.

For registration purposes, both the CT and the CBCT were re-sampled into voxels of the size of one cubic millimeter. In the experiments we presented in this paper, pelvis data were cropped around the clinically relevant volume, which included the prostate (and the surrounding PTV), the bladder, and the rectum. The segmentation results via level set models were converted into volumes in the format of binary voxel arrays. The segmented regions in CT images were assumed to be accurate since they were obtained from the CT, which has less noise and better contrast. In addition, the CT segmentation is part of the planning process, which usually does not have a time restriction, as does CBCT segmentation. Therefore the results can undergo extra improvement procedure, whether automatic or manual-based, before the registration.

The meshless model of each object is composed of sampling points on the surface of the corresponding level-set-segmented volume. During the registration, we denote the displacement at each sampling point as a combination of global motion and local deformation. To determine the global motion in the current iteration, we minimize the moving least square error at each point:

$$\sum_i w_i |f_p(u_i) - v_i| \tag{2}$$

where u_i are initial location vectors of sampling points, v_i are location vectors of sampling points in the current iteration of the registration, f_p is the global transformation functions at points of evaluation, and w_i are weights dependent on the location of the point of evaluation p. In our approach, the points of evaluation are more densely (compared to the sampling points) sampled on the surface of the segmented clinical object. We define the global motion at these points in the form of an affine transformation so that

$$f_p(u_i) = u_i \mathbf{M} + \mathbf{T} \tag{3}$$

Define $u_* = \frac{\sum_i w_i u_i}{\sum_i w_i}$ and $v_* = \frac{\sum_i w_i v_i}{\sum_i w_i}$, and also $\hat{u_i} = u_i - u_*$ and $\hat{v_i} = v_i - v_*$, we can solve $\mathbf{M}$ and $\mathbf{T}$ using

$$\mathbf{T} = v_* - u_* \mathbf{M} \tag{4}$$

$$\mathbf{M} = (\sum_i \hat{u_i}^T w_i \hat{u_i})^{-1} \sum_j w_j \hat{u_j}^T \hat{v_j} \tag{5}$$

The computational process for the global motion (i.e., **M** and **T**) is time efficient since the locations of u_i are fixed during the registration so that it is possible to pre-compute some parts in equation 5 to promptly yield the global motion. The computed global motion will be used as a global constraint to the registration. The global constraints at points of evaluation are treated same as 'demons' forces generated using local pixel gray scale. Both forces will undergo a diffusion process to redistribute to every pixels in the image to be registered. We changed the original equation of the registration force in Demons algorithm

$$\boldsymbol{u_{local}} = (m - s) \times \left(\frac{\boldsymbol{\nabla} s}{|\boldsymbol{\nabla} s|^2 + \alpha^2 (s - m)^2} + \frac{\boldsymbol{\nabla} m}{|\boldsymbol{\nabla} m|^2 + \alpha^2 (s - m)^2} \right) \tag{6}$$

by adding the global constraint in the region of the meshless model so that the global and local influences work together to guide the registration process.

$$u_{all} = \lambda_{local} u_{local} + \lambda_{global} u_{global} \tag{7}$$

where u_{global} is derived from equation 5 via the diffusion, and λ are weights. We set a threshold on the number of loops required by the registration, usually 100.

2.3 Meshless Segmentation in CBCT

The registration generated the displacement and hence the correlation between the CT and CBCT, as well as meshless models registered into the CBCT domain. To further improve the accuracy of the convergence between the registered and the reference image. The meshless models underwent another round of local deformation process. Each node of the meshless model deformed under the influence of the image features in the CBCT data, but their deformations were constrained by the internal structural constraint of each meshless model and the external constraint between models. After all model nodes arrived at equilibrium points in the CBCT domain, we computed the local deformation at pixels belonging to the volume of the model. The displacement at each pixel was calculated by minimizing the residue moving least square errors at points of evaluation. To improve the efficiency, we can use the same pre-computed kernel in the registration by using the same set of the sampling points.

$$\sum_i w_{ij} |p_j - q_i| \tag{8}$$

where q_i are the local deformations at the sampling points of the meshless model, p_j are the displacements to be decided at object surface points of evaluation j, w_{ij} are weights based on the relative distance between the pixel and model nodes. The local deformation process was equal to the segmentation of the object in the CBCT, and also helped to improve the registration between the CT and CBCT.

3 Experiments and Validation

The proposed segmentation-registration-segmentation framework has been tested on 15 data sets, each including both the planning CT and the treatment CBCT from prostate cancer patients. CT image volumes were acquired from a Philips CT scanner, while the CBCT data were acquired using a Varian On Board Imaging (OBI) system for patients treated by linear accelerators. The original pixel size for the CT data is a fixed $0.94 \times 0.94 \times 3$mm, but the original pixel size for CBCT images varies. The CT segmentation and validation take place in the original CT image domain. The registration, the CBCT segmentation, and the validation of both take place in the re-sampled image domain (1 by 1 by 1mm).

First we show the experimental results of CT segmentation. The segmentation results were compared with manual segmentations. The segmentation quality was evaluated based on the similarity between the manual segmentation and the proposed segmentation method. We focused on the volumetric evaluation, which was more relevant to the calculation of dose distribution, and was more critical in IGRT. The three measurement we used were the False Positive (FP), False Negative (FN), and True Positive (TP) of the pixels in the segmentation results, using the manual segmentation as the ground truth. The final volume similarity is computed using $S_{vol} = \frac{2TP}{2+FP-FN}$. An average of 93.2% volume similarity has been achieved for CT segmentation in 15 cases. The registration was evaluated by measuring the difference between the registered volume (from CT segmentation with manual revisions) and manual segmentation in the CBCT data. It is shown in Table. 1 that after the registration, the registered volumes retain a volumetric similarity of 91% to the manual segmentations of prostates in CBCT. For bladders and rectums, the volumetric similarities are less, but the averages are still over 85%. Some results are shown in Fig.1 and Fig.2.

The CBCT segmentation used the registration results to determine the initial location and shape of meshless deformable models. The segmentation results underwent a validation process similar to the CT segmentation. To verify the impact of the accuracy of CT segmentation on the final outcome, we used both manual and automatic CT segmentations as the input for the registration and compared the quality of the final CBCT segmentation. An average of 95% volumetric similarity was achieved using the manual CT segmentation as the input for the CT-CBCT registration. The average volumetric similarity was slightly lower at 93% when we use automatic CT segmentations.

The proposed framework is implemented on a Dell Server PE2900 with Xeon 2.66GHz CPU and 8GB RAM using Matlab. The implementation is highly time-efficient. The CT segmentation takes less than 3 minutes to segment the prostate, bladder, and rectum simultaneously. The registration of a cropped region of interest between the CT and CBCT domain takes 38 second in average for 15 cases. The CBCT segmentation takes less than one minute for the convergence between models and desired image features. The framework also needs extra time for the preprocessing of images, this usually takes another few more minutes depending on the user proficiency. Notice in IGRT there is no time restriction on

Table 1. The overall performance for prostate segmentation and registration. Column 'CT' are similarity measures of the automatic CT segmentation results against manual CT segmentations. CT Time is the time needed for CT segmentation. Column 'Registration' shows the similarity measures of the registered automatic CT segmentations against manual CBCT segmentations. Column 'CBCT' shows the similarity measure for automatic CBCT segmentations against manual CBCT segmentations.

data	CT	CT Time	Registration	Reg. Time	CBCT	CBCT Time
Set1	96%	152sec	91%	39sec	93%	57sec
Set2	92%	146sec	90%	42sec	92%	59sec
Set3	97%	137sec	94%	41sec	95%	58sec
Set4	94%	151sec	90%	35sec	92%	45sec
Set5	93%	120sec	91%	36sec	93%	48sec
Set6	91%	144sec	90%	40sec	93%	57sec
Set7	94%	141sec	92%	38sec	93%	50sec
Set8	89%	165sec	87%	37sec	89%	49sec
Set9	95%	138sec	90%	33sec	92%	42sec
Set10	90%	171sec	86%	39sec	90%	51sec
Set11	95%	152sec	92%	40sec	94%	53sec
Set12	93%	155sec	94%	36sec	95%	48sec
Set13	94%	146sec	95%	37sec	95%	47sec
Set14	95%	148sec	92%	36sec	94%	42sec
Set15	90%	160sec	91%	44sec	95%	61sec

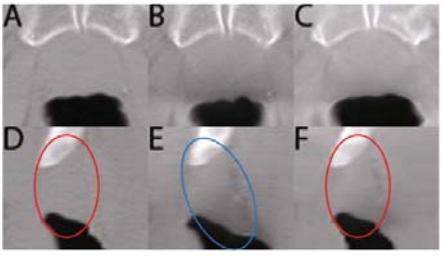

Fig. 1. Transverse and sagittal view of the registration results in the cropped image volume around the prostate. A, D are reference CT planning data; B, E are target CBCT images; and C, F shows the registered CBCT data. In D, E, F, the prostate regions are circled to show the motion in the Superior/Inferior direction.

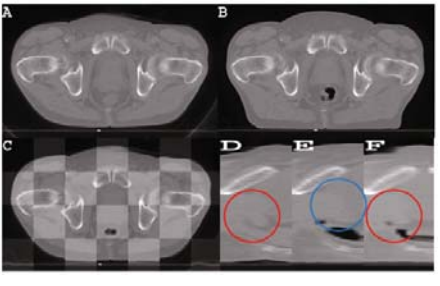

Fig. 2. Whole body registration of pelvis data. A, D are reference images; B, E are views of the target; C is a check display of the registration with registered image superimposed with the reference; and in D, E, F the prostate areas are circled out to show the motion in the Superior/Inferior direction.

CT preprocessing and segmentation. Therefore for each new treatment CBCT, with the help of previous CT segmentation, we can have clinical relevant objects registered and delineated in less than two minutes.

4 Conclusion

We have proposed a fast segmentation-registration-segmentation framework for the analysis of CBCT treatment data in IGRT. The overall accuracy of the framework is over 90% measured in shape similarity. The framework is capable of generating segmentation results in CBCT data in less than two minutes, which may inspire more IGRT applications with clinical importance.

References

1. Jemal, A., Siegel, R., Ward, E., Hao, Y., Xu, J., Murray, T., Thun, M.J.: Cancer statistics, 2008. CA Cancer J. Clin. 58(2), 71–96 (2008)
2. Purdy, J.A.: Intensity-modulated radiation therapy. Int. J. Radiat. Oncol. Biol. Phys. 35(4), 845–846 (1996)
3. Xing, L., Cotrutz, C., Hunjan, S., Boyer, A.L., Adalsteinsson, E., Spielman, D.: Inverse planning for functional image-guided intensity-modulated radiation therapy. Phys. Med. Biol. 47(20), 3567–3578 (2002)
4. Yue, N.J., Kim, S., Jabbour, S., Narra, V., Haffty, B.G.: A strategy to objectively evaluate the necessity of correcting detected target deviations in image guided radiotherapy. Med. Phys. 34(11), 4340–4347 (2007)
5. Betrouni, N., Dewalle, A.S., Puech, P., Vermandel, M., Rousseau, J.: 3d delineation of prostate, rectum and bladder on mr images. Comput. Med. Imaging Graph 32(7), 622–630 (2008)
6. Costa, M.J., Delingette, H., Novellas, S., Ayache, N.: Automatic segmentation of bladder and prostate using coupled 3d deformable models. In: Med. Image Comput. Comput. Assist. Interv. Int. Conf., vol. 10(pt. 1), pp. 252–260 (2007)
7. Davis, B.C., Foskey, M., Rosenman, J., Goyal, L., Chang, S., Joshi, S.: Automatic segmentation of intra-treatment ct images for adaptive radiation therapy of the prostate. In: Med. Image Comput. Comput. Assist. Interv. Int. Conf., vol. 8(Pt 1), pp. 442–450 (2005)
8. Greene, W.H., Chelikani, S., Purushothaman, K., Chen, Z., Knisely, J.P., Staib, L.H., Papademetris, X., Duncan, J.: A constrained non-rigid registration algorithm for use in prostate image-guided radiotherapy. In: Med. Image Comput. Comput. Assist. Interv. Int. Conf., vol. 11(Pt 1), pp. 780–788 (2008)
9. Brock, K.K., Nichol, A.M., Menard, C., Moseley, J.L., Warde, P.R., Catton, C.N., Jaffray, D.A.: Accuracy and sensitivity of finite element model-based deformable registration of the prostate. Med. Phys. 35(9), 4019–4025 (2008)
10. Malladi, R., Sethian, J.A.: Image processing via level set curvature flow. Proc. Natl. Acad. Sci. U S A 92(15), 7046–7050 (1995)